NIEND: Neuronal Image Enhancement through Noise Disentanglement

Zuo-Han Zhao, Yufeng Liu*

SEU-ALLEN Joint Center, Institute for Brain and Intelligence, Southeast University, Nanjing, 210036, China

*To whom correspondence should be addressed.

Abstract

Motivation

The full automation of digital neuronal reconstruction from light microscopic images has long been impeded by noisy neuronal images. Previous endeavors to improve image quality can hardly get a good compromise between robustness and computational efficiency.

Results

We present the image enhancement pipeline named Neuronal Image Enhancement through Noise Disentanglement (NIEND). Through extensive benchmarking on 863 mouse neuronal images with manually annotated gold standards, NIEND achieves remarkable improvements in image quality such as signal-background contrast (40-fold) and background uniformity (78-fold), compared to raw images. Furthermore, automatic reconstructions on NIEND-enhanced images have shown significant improvements compared to both raw images and images enhanced using other methods. Specifically, the average F1 score of NIEND-enhanced reconstructions is 0.88, surpassing the original 0.78 and the second-ranking method, which achieved 0.84. 52% of reconstructions from NIEND-enhanced images outperform all other 4 methods in F1 scores. In addition, NIEND requires only 1.6s on average for processing 256×256×256-sized images, and images after NIEND attain a substantial average compression rate of 1% by LZMA. NIEND improves image quality and optimizes the neuron reconstruction process, providing potential for significant advancements in automated

neuron morphology reconstruction of petascale.

Availability and Implementation

The study is conducted based on Vaa3D and Python 3.10. Vaa3D is available on GitHub (https://github.com/Vaa3D). The proposed NIEND method is implemented as a Python source, hosted on GitHub along with the testing code and data (https://github.com/zzhmark/neuron-image-denoise-exp). The raw neuronal images of mouse brains can be found at the BICCN's Brain Image Library (BIL) (https://www.brainimagelibrary.org).

1 Introduction

The advent of high-resolution whole-brain light microscopy has instigated a transformative shift in neuroscience, equipping researchers with the capability to visualize and scrutinize the neuronal connectome at the mesoscale level (Jiang, Gong and Yuan 2023). However, the immense volume of whole-brain images and the complex nature of axonal arborizations present significant obstacles in capturing neuron morphology (Liu *et al.* 2022). The process of manual reconstruction, a meticulous task of extracting morphology from images, is notably labor-intensive. The potential of automated algorithms to expedite this process is widely acknowledged (Peng *et al.* 2015; Liu *et al.* 2022). Yet, their efficacy remains limited due to their vulnerability to different types of noise and the subpar quality of neuron optical image data (Guo *et al.* 2022).

The majority of noises can be traced back to various factors that occur during the image acquisition process. These factors encompass a broad spectrum of issues, including residual modulation artifacts (Zhong *et al.* 2021), artifacts produced by slicing or chemical washing (Zhu *et al.* 2017), and light scattering throughout the brain tissue (Zhu *et al.* 2017). Out-of-focus light or flare originating from proximate neurites and high-intensity soma can further contribute to the fuzziness on their surface (Zhong *et al.* 2021). It is worth noting that in the context of MOST (Micro-optical Sectioning Tomography) techniques that utilize serial sectioning (Li *et al.* 2010; Gong *et al.* 2013, 2016), these artifacts can display an asymmetric distribution and attenuating in a direction (attenuation noise) opposite to the sectioning (**Figure**

1a). During the post-processing of whole-brain images, the amalgamation of different image tiles acquired under slightly varying conditions can lead to abrupt boundaries (**Figure 1b,c**). Besides, auto-fluorescent substances or self-illuminating tissues may exhibit brightness levels that are on par with neurites in the neuron optical image (**Figure 1d**).

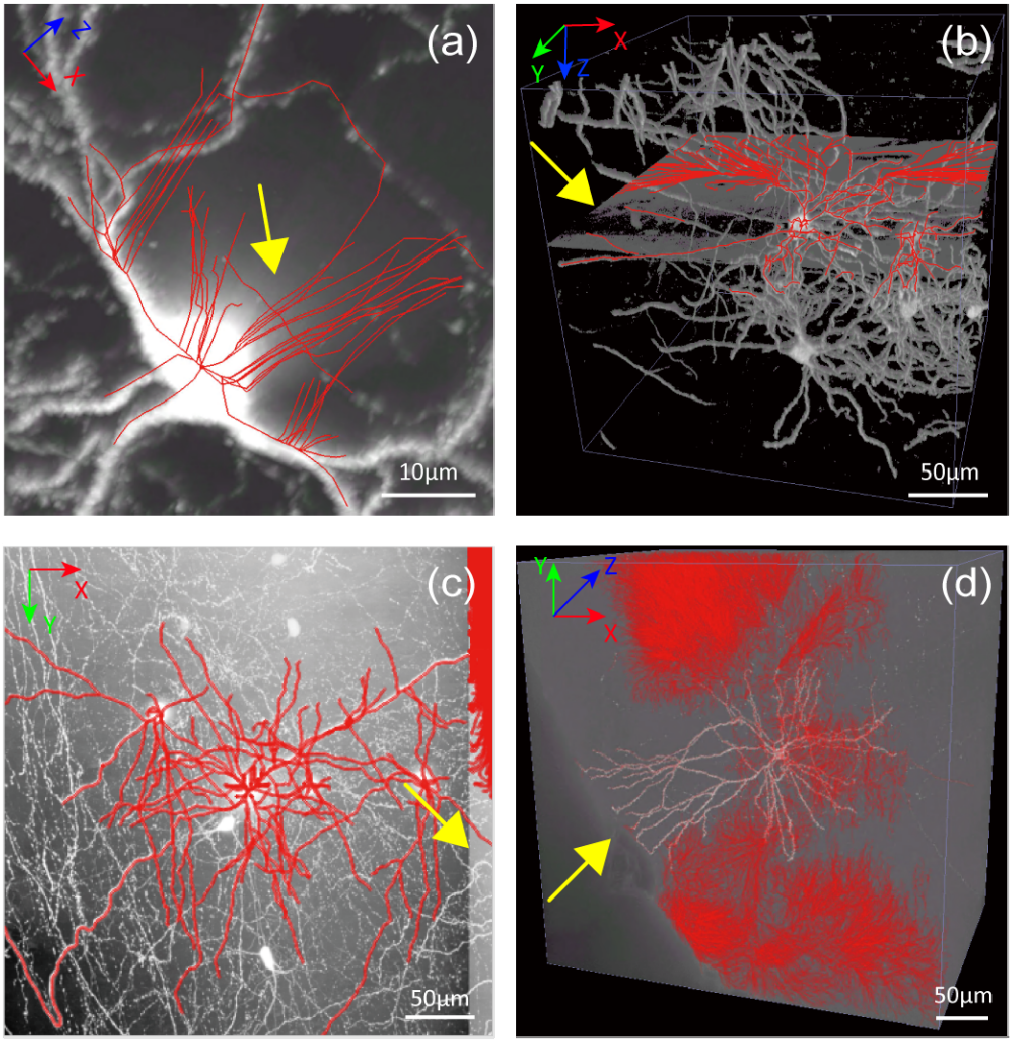

***Figure 1*. Depiction of prevalent noise types in neuron optical images obtained via light microscopy**. Each image is superimposed with reconstructions generated via automatic tracing (utilizing APP2, with

default parameters). (**a**) the maximum intensity projection (MIP) of a neuronal image block displaying an attenuating fuzziness along the opposite sectioning direction, a diffusive artifact typically observed near the soma. (**b**) A 3D perspective of an image block highlighting isolated boundary artifacts, identified by abnormal illusion within a plane. Thresholding is applied to the image for better visualization. (**c**) MIP view of a block depicting boundary artifacts between heterogeneous tiles, manifesting as unnatural intensity shifts orthogonal to one axis. A sigmoid enhancement was applied to highlight the artifact. (**d**) pervasive background noises.

Numerous endeavors have been made to reduce noise in neuron optical images, thereby enhancing the performance of automatic tracing. Apart from general-purpose techniques derived from conventional image processing, such as signal filtering and deep learning (Qi *et al.* 2022), specialized tools tailored for neuron images have been developed to tackle specific noise types (Smith *et al.* 2015; Chernavskaia *et al.* 2017; Peng *et al.* 2017). Several methods exploiting the tubular attributes of neurites have been innovated to amplify the neurite (Hayman *et al.* 2004; Meijering 2010; Mukherjee and Acton 2015; Zhou *et al.* 2015). Given the notable trade-off between the efficiency and specificity of previous techniques, a signal processing pipeline composed of only classical image filters has substantially improved signal enhancement with high efficiency (Guo *et al.* 2022). However, these methods are still imperfect and suffer from either low robustness or high computational complexity, necessitating a swift algorithm that can address image quality issues while maintaining reasonable computational resource demands. With the constant surge in the generation of high-resolution whole-brain

images for mammals or primates at the petascale, the urgency for such an accurate, robust denoising algorithm that offers affordable computation is escalating.

In this study, an effective and computationally efficient method is proposed to address the aforementioned various quality issues combinatorically, named Neuronal Image Enhancement through Noise Disentanglement (NIEND). Our results show that more than significantly suppressing the noise, NIEND improves intensity inhomogeneity among neurites and their dimness in distal regions, achieving superior enhancement than previous methods. By avoiding sophisticated methods to detect neuron structures and utilizing straightforward filters, NIEND minimizes computational costs. Its performance has been verified using manually annotated reconstructions and benchmarked against previous methods, showing considerable promise for large-scale processing of neuron optical images and achieving significant improvements.

2 Materials and Methods

2.1 Dataset

The study is predicated on the 3D neuron optical image blocks obtained from 39 whole mouse brain images (**Supplementary Data**) acquired through the fMOST systems (Gong *et al.* 2013, 2016), accompanied by 1891 manually annotated single neuron reconstructions released by SEU-Allen Joint Center (Peng *et al.* 2021). The image resolution varies laterally from 0.20 to 0.35μm/pixel while maintaining a consistent resolution of 1μm/pixel in the axial direction. The images were captured in 16-bit. We cropped image blocks measuring 1024×1024×256 (in

XYZ order) at the highest resolution of whole brain images for all neurons, with the soma centralized. This approximates a width ranging from 205μm to 358μm laterally and 256μm axially, containing most of the dendrites. These blocks are filtered for sparsity to facilitate the calculation of precision and recall rate of automatic tracing results. It is done by scrutinizing the presence of any significant neurite intersection from other neurons in maximum intensity projection (MIP) of the XY-plane to eliminate possible crossing artifacts that are out of scope for this study. Finally, a total of 863 neurons remain. Manual reconstructions (gold standards) were cropped accordingly, with any suspending structures (those with parent structures outside the block) removed.

2.2 Overview of NIEND Pipeline

The NIEND pipeline is composed of three key modules: high-pass filtering, intensity shifting, and low-pass filtering (**Figure 2**). The composite high-pass filtering module is a collection of high-pass filters that incorporates multiple filters to combat various types of low-frequency noise. In this study, we showcased two filters—the diffusion filter and the orthogonal filter—to mitigate the attenuation noise (**Figure 1a**) and low-frequency artifacts of large bulks (**Figure 1b,c**). Although many high-pass filtered images can be well-refined (**Supplementary Figure 1d**), there are considerable leftover noises that require subsequent processing, and their intensities (values of voxels) are heterogeneously distributed across blocks. Therefore, an instance-aware intensity shifting is employed to adaptively map these inhomogeneous intensities to the unsigned 8-bit domain, to standardize and minimize the inhomogeneity across

different neurons. Finally, a wavelet filter is adopted as a low-pass filter to mitigate remaining high-frequency noises.

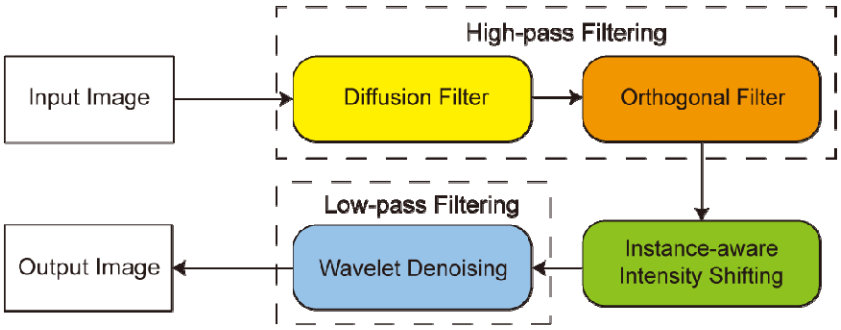

***Figure 2*. Schematic representation of the NIEND pipeline.** This diagram presents a simplified flow of the NIEND, starting from the input image. The initial processing stage is a high-pass filtering module that integrates two filters: the diffusion filter and the orthogonal filter. These filters are engineered to eliminate diffusive halo artifacts along the Z dimension (the opposite direction of sample sectioning) and to remove large bulks of orthogonally situated noise respectively. Subsequent steps include instance-aware intensity shifting and wavelet denoising, which refine the high-pass filtered result by adjusting the image intensity range and eliminating potential high-frequency noise.

2.3 Noise-specific high-pass filtering

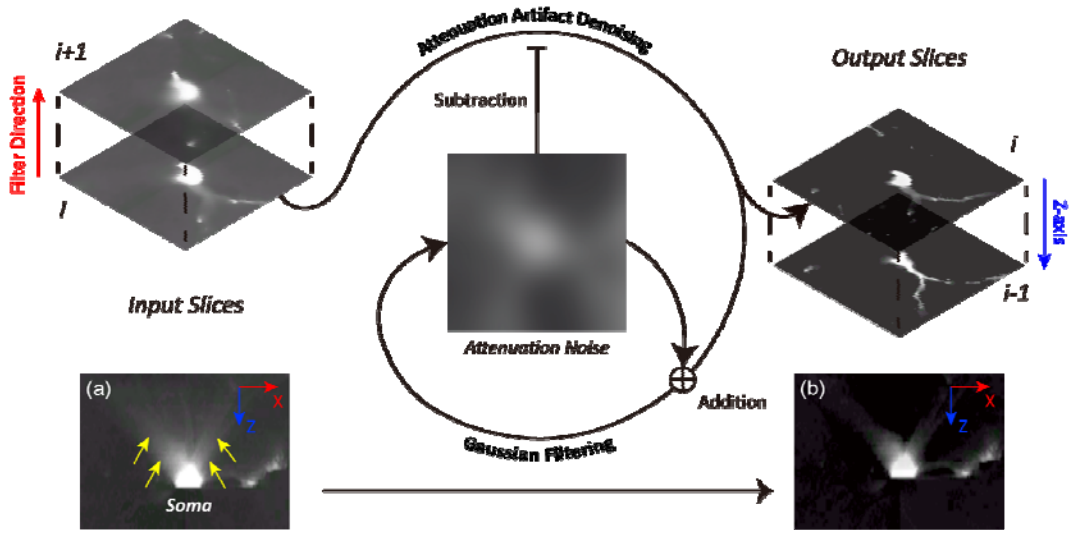

***Figure 3*. Diagrammatic representation of the diffusion filter.** The filtering sequentially subtracts an updating slice of attenuation noise from each raw image slice along its Z-axis, typically the sectioning direction. During each iteration, the attenuation noise is updated by merging with the denoised output of this iteration and implementing Gaussian blurring. (**a**) an XZ slice of an input image, with the highlight of the diffusion artifact extending along the Z-axis and dispersing over the X-axis (yellow arrows). (**b**) the processed image where the artifact is significantly reduced.

The high-pass filtering stage stands out as the most critical step, as it primarily tackles the low-frequency noise and artifacts that misled automatic tracing into serious over-tracing. It is started by a diffusion filter (**Figure 3**) that estimates the neurite signal based on a self-iterating, feedback model. The asymmetry of the attenuation noise (**Figure 1a**) allows the estimation ($\boldsymbol{est_n}$) to propagate slice by slice along the Z dimension. For each output slice, the current raw input slice ($\boldsymbol{raw_n}$) is used as the input and previous output slices can be regarded as sources of

noise (**Equation 1.1.1**). Assuming the sources to be additive and attenuating solely dependent on their distances (***dist$_i$***) to the plane under examination (**Equation 1.1.2**), the noise attenuation can be simplified as Gaussian diffusion (**Equation 1.2**) in the XY-plane with its sigma escalating linearly with ***dist$_i$***, given the uniform interval between slices (**Equation 1.3.1**). The parameter $\boldsymbol{\sigma}$ is determined as inversely proportional to the lateral resolution of the image (**Supplementary Table 1**). Then, each Gaussian diffusion function is restructured into an iterative convolution (**Equation 1.3.2**) of a common Gaussian kernel (***G$_\sigma$***). This convolution is referred to as the attenuation noise (***noise$_n$***) in the context of this study (**Equation 1.3.3**).

$$est_n = raw_n - Attenuation(est_{n-1}, est_{n-2}, \dots, est_1) \#(1.1.1)$$

$$= raw_n - \sum_{i=1}^{n-1} F(est_i, dist_i) \qquad \#(1.1.2)$$

$$G_\sigma(x, y) = \frac{1}{2\pi\sigma^2} e^{-\frac{x^2+y^2}{2\sigma^2}} \#(1.2)$$

$$est_n = raw_n - \sum_{i=1}^{n-1} est_i(x, y) * G_{(n-i)\sigma} \qquad \#(1.3.1)$$

$$= raw_n - \sum_{i=1}^{n-1} \left(est_i * \prod_{j=1}^{n-i} G_\sigma \right) \#(1.3.2)$$

$$= raw_n - noise_{n-1} \qquad \#(1.3.3)$$

The attenuation noise can be computed from its last iteration (**Equation 1.4**), obviating the summation through all of the previous estimations.

$$
\begin{aligned}
noise_n &= \sum_{i=1}^{n-1}\left(est_i * \prod_{j=1}^{n-i} G_\sigma\right) \\
&= G_\sigma * \left(est_{n-1} + \sum_{i=1}^{n-1-1}\left(est_i * \prod_{j=1}^{n-i} G_\sigma\right)\right) \\
&= G_\sigma * (est_{n-1} + noise_{n-1}) \#(1.4)
\end{aligned}
$$

The final iteration equations are packed in **Equation 1.5**. Here, a multiplier ***α(n)*** is incorporated into the attenuation noise to dynamically normalize its strength to match the average intensity (***Mean***) of the estimated attenuation noise with that of the input slice. This multiplier also comprises ***k*** (set as 0.9) as a parameter to mitigate the performance of this filter, in case it might excessively undermine the foreground.

$$
\begin{cases}
est_n = raw_n - \alpha(n) \cdot noise_{n-1} \\
\alpha(n) = k \cdot \dfrac{Mean(raw_n)}{Mean(noise_{n-1})} \\
noise_n = G_\sigma * (est_{n-1} + noise_{n-1})
\end{cases}
\#(1.5)
$$

Subsequently, an orthogonal filter is applied. For each slice (XY-plane), the filter first averages the intensity over the X-axis and the Y-axis respectively to get two vectors. Then, a direct sum is computed by adding the elements from the two vectors combinatorically and removed from the input slice. This filter is designed to counteract the boundary artifact between tiles of images, which are situated orthogonally. It can also counteract other artifacts of large sizes, such as stripe-like sinusoidal noise of large sizes (**Supplementary Figure 1**) and unwanted brain

tissues (**Supplementary Figure 4**). The schematics and results of each step are also depicted in **Supplementary Figure 1**, beginning with the raw image.

2.4 Instance-aware intensity shifting

The purpose of instance-aware intensity shifting is to locate the optimal dynamic range of voxel intensities and standardize them to a more consistent distribution across images. In the meantime, since most tracing algorithms require input images of 8-bit depth, the shifting also enables a high-fidelity conversion for images of higher depth.

The intensity range of the image is clipped as a start. Then, the image is linearly rescaled and converted to 8-bit at the same time. The lower limit bound is set by percentile thresholding. Given the sparse nature of neuron optical images, a large portion of the image volume can be nullified. Empirically, a percentile around 1.0% is practical for a dendrite block of sub-micrometer resolution. In this study, minor adjustments (±0.5%) are made for images originating from brains of varying resolutions (**Supplementary Table 1**). The upper limit is determined as half of the maximum intensity of the neuron soma, i.e. the maximum intensity of a center sub-block (the soma is centered in our image blocks) of size 128×128×32 voxels in the highest resolution image, i.e. 25.6×25.6×32–44.8×44.8×32μm^3. Any intensity exceeding this threshold will be capped. Sometimes, the upper threshold computed from the soma intensity can approximate or fall lower than the percentile threshold, so the final upper threshold will be

guaranteed to be at least 256 (the total number of grayscales in an 8-bit image) above the lower threshold.

2.5 Wavelet low-pass filtering

High-frequency noise, including remnants of artifacts left by previous steps, can be amplified during the intensity shifting as a side effect (**Supplementary Figure 2a**). However, considering the high-frequency characteristics of neuronal structures, the application of any low-pass filter can introduce undesirable degradation at the same time.

Here, we choose wavelet denoising for a balance between denoising and degradation. It targets the glitching artifacts (1–2 voxels of abruptly high intensity) that are common only for the high-frequency noise rather than the neurite signal and even mends minor neurite breakages, which can be regarded as an inverted case of glitching artifacts (**Supplementary Figure 2c**), i.e. 1–2 voxels of abruptly low intensity.

In this research, given that the lateral resolution is significantly greater than the axial (Halidou *et al*. 2023), wavelet denoising is approximated as a slice-by-slice process to minimize memory usage. The Haar wavelet and hard thresholding are adopted. The wavelet level is capped at 2. The thresholds for each wavelet level are adaptively estimated by BayesShrink (Chang, Bin Yu and Vetterli 2000).

2.6 Benchmarking

The study processes image blocks from 863 sparsely labeled neurons using NIEND and various comparative techniques, including adaptive thresholding (which subtracts the average intensity of neighboring voxels), multiscale enhancement (Zhou *et al.* 2015), and Guo's enhancement method (Guo *et al.* 2022). The reconstruction of neurons is conducted through all-path-pruning 2 (APP2) (Xiao and Peng 2013), with the default parameter settings.

The comparison of image quality involves the calculation of signal-background contrast (SBC) and within-image homogeneity (WIH) on both the foreground and the background for each image (Guo *et al.* 2022). For each neuron, the foreground is estimated as a neuronal mask derived from its radius-profiled manual reconstruction, while the background is the difference between the neuronal mask of twice the profiled radii and the foreground mask. The SBC is then estimated as the ratio between the median of the foreground and the median of the background (**Equation 2.2**). The WIH of the background is computed as the entropy (**Equation 2.3**) and the uniformity (**Equation 2.4**), while the WIH of the foreground is computed as the relative standard deviation (RSD) (**Eq. 2.5**). These metrics have been modified to avoid zero denominators.

$$sbc(fg, bg) = \frac{median(fg)}{median(bg) + 1} \#(2.2)$$

$$ent(p) = -\sum_i p(i) \log p(i) \#(2.3)$$

$$uni(p) = \sum_i p(i)^2 \#(2.4)$$

$$rsd(fg) = \frac{std(fg)}{median(fg) + 1} \#(2.5)$$

The precision and recall metrics are computed for every neuronal block. These calculations are based on the Percent of Different Structures (PDS) metric (Peng, Long and Myers 2011; Xiao and Peng 2013), a rate that measures the percentage of deviated lengths of a neuron tree against a reference tree (**Equation 2.6**). When the neuronal reconstructions are reverted to voxels, the deviated length is identified as the voxels where the distance to the nearest reference voxel surpasses a defined limit (**Equation 2.7**). Here, this limit is specified as 15 pixels (i.e. approximately 3μm).

$$PDS(neuron, neuron_{ref}) = \frac{Length\left(neuron - neuron_{ref}\right)}{Length(neuron)} \times 100\% \#(2.6)$$

$$neuron - neuron_{ref} = \left\{n_1 | min\{dist(n_1, n_2)\} > thr, n_1 \ in \ neuron, n_2 \ in \ neuron_{ref}\right\} \#(2.7)$$

The precision metric is calculated from the error, i.e., the PDS of the reconstruction against the gold standard (**Equation 2.8**). Conversely, the recall is determined as the PDS of the gold

standard against the reconstruction (**Equation 2.9**). Based on them, the F1 score is also computed. The distribution of these metrics is then compared across different methods in the dataset consisting of 863 sparse neuronal images.

$$precision = 1 - error$$
$$= 1 - PDS(neuron, neuron_{\mathrm{ref}}) \#(2.8)$$

$$recall = PDS\left(neuron_{ref}, neuron\right) \qquad \#(2.9)$$

In addition, the optimal image depths (estimated by comparing the tracing metrics) are adopted for each technique. The 8-bit version is used for multiscale enhancement and Guo's method, while the 16-bit version is used for the remaining methods. It is worth noting that APP2 will automatically convert the image to 8-bit before tracing. Running time and memory usage tests are conducted on 30 randomly sampled image blocks serially, with the first 10 results discarded to prevent initialization bias. The running time and memory usage are also acquired for image blocks of a more regular size (256×256×256). The smaller blocks are cropped from the center of the 1024×1024×256-sized blocks.

3 Results

3.1 NIEND improves the image quality substantially

We showcased the outputs of different NIEND steps with several examples containing typical

noises and artifacts discussed (**Figure 4**). The application of high-pass filtering significantly reduced the image noise and artifacts while retaining the neurite signals (**Figure 4b**). After the intensity shifting, the neurite structures are accentuated (**Figure 4c**), albeit with an increase in some of the residual noises, which are then mitigated with wavelet denoising (**Figure 4d**).

More comparisons between the input and output of NIEND are provided to comprehensively demonstrate the capabilities of NIEND (**Figure 4e–h**). It effectively eradicates substantial quantities of non-neuron artifacts, such as the illuminated brain tissue background (**Figure 4e,f**) and the sinusoidal band (**Figure 4g,h**). Several other types of issues that pose challenges for tracing are also addressed, such as poor contrast between the cells and background (**Figure 4e**), thin and dim local axon (**Figure 4f**), and broad dispersion between the foreground structures (**Figure 4g,h**).

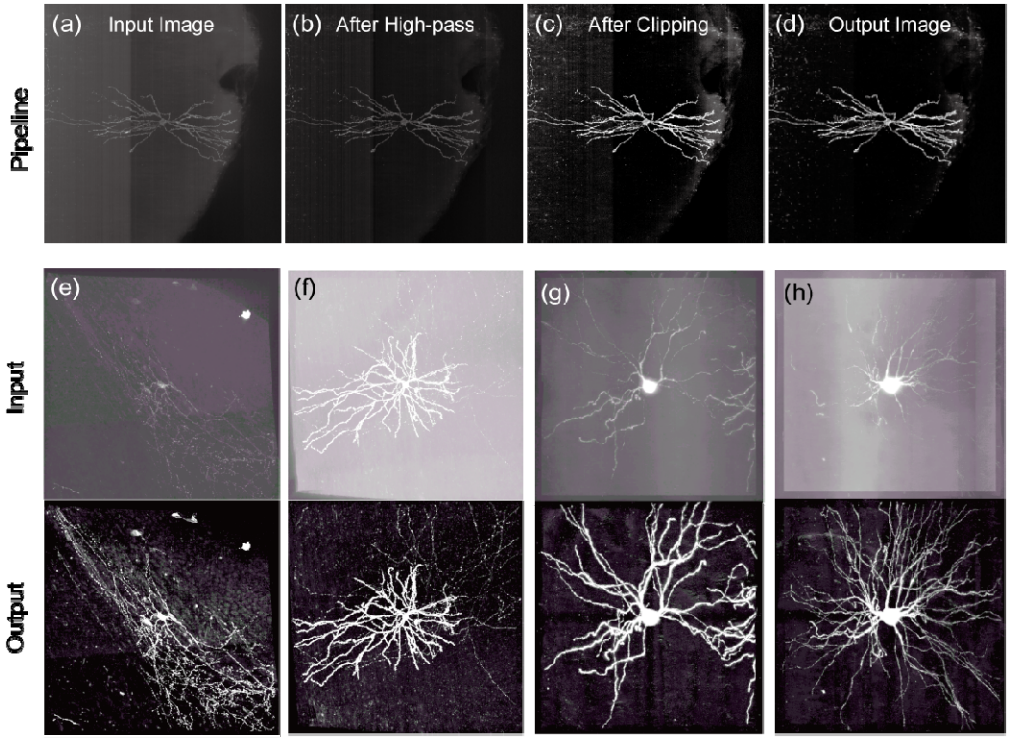

***Figure 4*. Examples of images after NIEND processing.** (**a–b**) An example case in MIP that demonstrates the outputs at each stage of the proposed pipeline. This encompasses the initial input image (**a**), the image after high-pass filtering (**b**), the image after instance-aware intensity shifting (**c**), and the final output image (**d**). (**e–h**) Comparison of another four initial (input, top) and final images (output, down) pairs using NIEND.

3.2 Comparison with other image enhancements

We further compared the performance of NIEND with existing state-of-the-art methods, including adaptive thresholding (AdaThr), multiscale enhancement (Multiscale), and Guo's enhancement method (Guo). The classic methods like the anisotropic filter and the Meijering filter, despite their power, are excluded for their extreme computational cost.

The advantages of NIEND are demonstrated with seven neuronal image blocks with representative noise types (**Figure 5**). Adaptive thresholding is a highly lightweight form of high-pass filtering. It excels at denoising while introducing significant side effects, including the increased emptiness of the soma center and fragmentation of nearby stems (**Supplementary Figure 3a**). Its isotropic, regular-shaped kernel provides no selectivity towards noise and artifacts and exterminates the signal of a rigid bandwidth that overlaps that of the neurite. Its over-denoising issue is particularly severe in high-quality images with highly illuminated and plump soma. It also fails to handle all kinds of boundary artifacts (**Supplementary Figure 3d**). In contrast, NIEND is capable of settling these issues (**Supplementary Figure 3b,e**) with a comparable denoising performance (**Figure 5e**). Multiscale enhancement effectively denoises the samples but results in a catastrophic loss when it misidentifies neurites as noise (**Figure 5e,f**), which occurs more frequently in images with large, noisy structures.

Guo's method is a competent enhancement tool for weak neurite signals. Still, its efficacy is limited when encountering high-intensity differences between neuronal structures (**Figure 5b,c**) or extremely low foreground intensity (**Figure 5a,g**). Guo's method aims to denoise the slowly varying background noise using high-pass filtering in Fourier space, but in cases of poor quality, non-neuron objects of irregular shapes can remain unaddressed (**Figure 5e**). Instead, NIEND demonstrates its ability to enhance weak signals, including weak axons (**Figure 5b**), neurites obscured by other brilliant illuminants (**Figure 5c**), and distal parts of neurites (**Figure 5d**). It increases the homogeneity of intensity among neurites as well (**Figure 5f**).

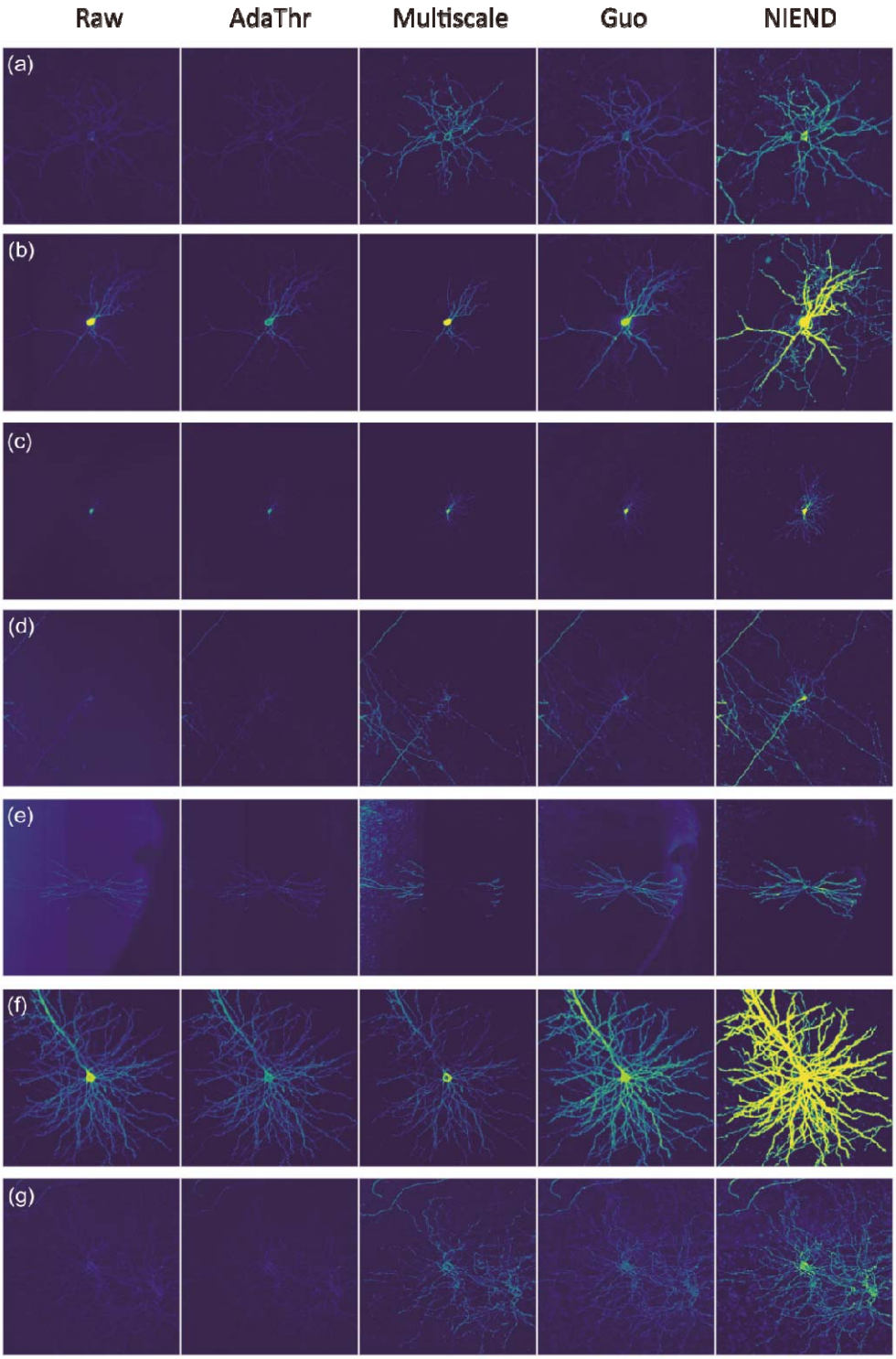

***Figure 5*. Comparative analysis of NIEND and preceding methods.** Each column represents one method, while each row represents a unique image sample. From left to right, the columns depict images without

processing (the raw image), after adaptive thresholding, after multiscale enhancement, after Guo's enhancement method, and after NIEND. Each of the samples represents a typical combination of noises: (**a**) a uniformly faint neuron with minimal noise. (**b**) a neuron featuring a pronounced soma and a faint axon. (**c**) a neuron with a noticeable soma and undetectable neurites. (**d**) a neuron set against a noisy backdrop, with barely discernible neurites. (**e**) a neuron embedded in a noisy brain tissue, characterized by conspicuous orthogonal and irregular boundaries. (**f**) a high-quality neuron with a significant intensity disparity between the soma and neurites. (**g**) a faint neuron entwined with another neuron.

A quantitative comparison is also conducted for quality improvement (**Figure 6**). The SBC serves as the primary indicator of enhancement. NIEND exhibits the most significant increase in SBC (40-fold), which is 15% higher than its nearest competitor, adaptive thresholding. In terms of background noise reduction, multiscale enhancement achieves the highest entropy reduction (58%) and the most remarkable increase in uniformity (178-fold). Despite modest improvement in entropy, NIEND secures the second-highest increase in background uniformity (78-fold), surpassing Guo's method, which trails behind by 5%. Contrary to the other indicators, an increase in the RSD of the foreground suggests higher signal loss. Multiscale enhancement demonstrates the highest escalation in RSD (11-fold) while NIEND only amplifies the RSD by 40%, the lowest among all. Overall, NIEND delivers the most significant and lossless enhancement in image quality.

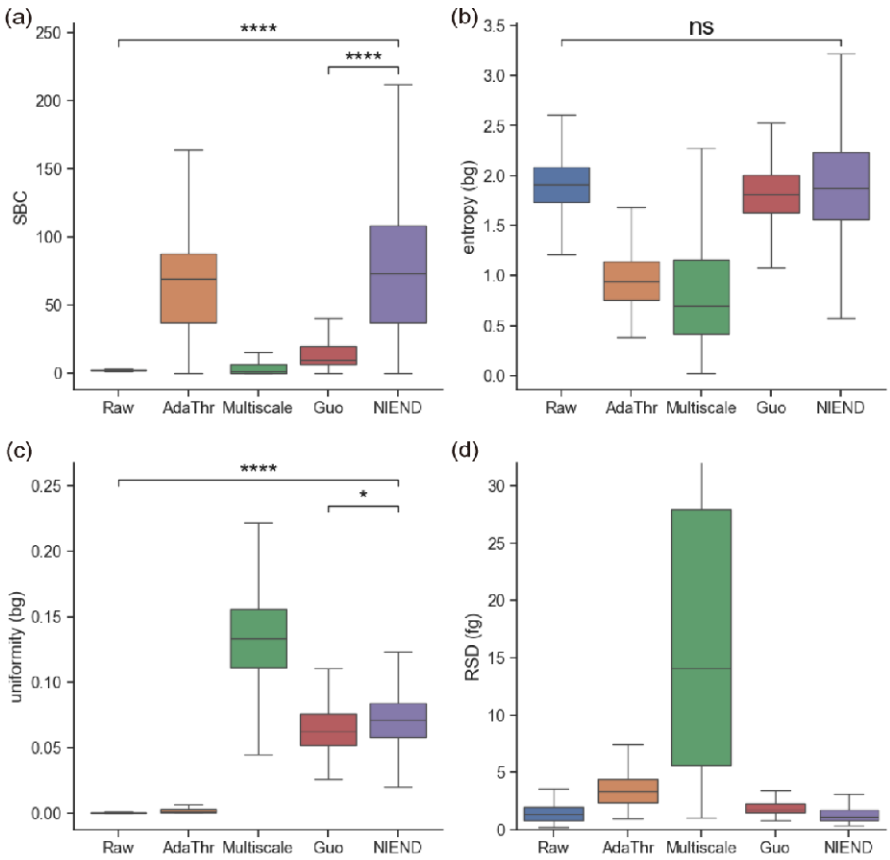

***Figure 6*. Quantitative evaluation of image quality after enhancement.** In each boxplot, the center line is the mean value, the box is bounded by Q1 and Q3, and the whiskers add 1.5-fold the interquartile range. (**a**) signal-background contrast. (**b**) background entropy. (**c**) background uniformity. (**d**) foreground relative standard deviation. These metrics collectively suggest that NIEND amplifies the signal prominence and uniformity more effectively than other comparative methods. Each statistical significance is obtained using the two-sided T-test.

3.3 NIEND improves automatic tracing

The performance of automatic tracing on the processed images is evaluated and benchmarked

across the image processing methods. **Figure 7** presents the tracing results of the same instances as organized in **Figure 5**. In line with conclusions drawn from the previous section, adaptive thresholding may impact the signals and incur the loss of numerous structures (**Figure 7b,d,g**); multiscale enhancement generally misses an even greater number of structures owing to tremendous signal loss. Guo's method delivers a substantial improvement in recall, but some samples exhibit over-tracing on unremoved noise or artifacts (**Figure 7e,g**). In contrast, NIEND outperforms in both avoiding over-tracing (**Figure 7d,e,g**) and retrieval of neurite structures (**Figure 7a,b,c**).

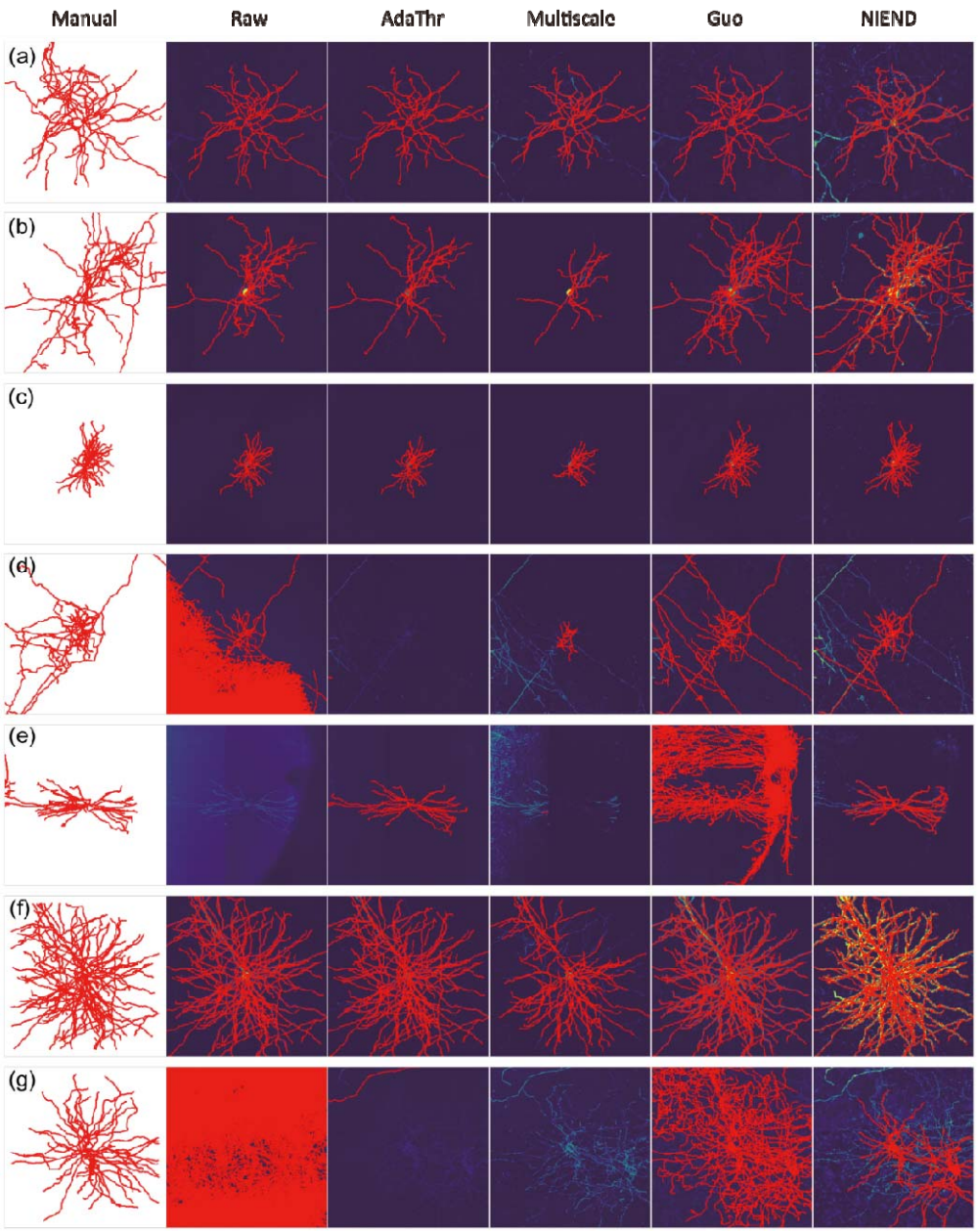

***Figure 7*. Comparative analysis of NIEND and previous methods for automatic tracing.** Each column represents one method, and each row corresponds to a unique image sample. The layout is analogous to that in **Figure 5**, except for the first column, which provides the gold standards of the neuron reconstructions. (**a**) Minimal differences among the results indicate APP2's competence in reconstructing weak signals, given the noise is trivial and the contrast between neurites is moderate in this case. (**b**) Complete axon reconstruction is

achieved exclusively with NIEND. (**c**) Dendrite is entirely reconstructed with a reduced intensity difference relative to the soma following the application of NIEND. (**d**) All of the methods aid in eliminating the artifact that could lead to over-tracing, yet the error and recall of the methods vary, with NIEND offering a balanced approach. (**e**) Adaptive thresholding proves the most efficient in resolving problematic backgrounds. (**f**) Despite the high image quality, full reconstruction is unattained solely for multiscale enhancement, indicative of its deficiency. (**g**) The signal, while uniformly weak, is close to the background, thereby posing a high risk of over-tracing. NIEND once again demonstrates its balanced precision and recall in such circumstances.

Figure 8 presents the analysis of the precision, recall, and F1 of the tracing results on the 863 sparse neurons. Our method exhibits notably higher F1 scores than the raw image, adaptive thresholding, and multiscale enhancement, and holds a statistically significant advantage over the second-best Guo's method (+4.4%). Adaptive thresholding and multiscale enhancement significantly outperform others in precision, but their recall performance drastically declines. NIEND achieves a recall rate comparable to Guo's method but offers superior precision (+4.3%), thus bringing a higher F1. The averages of these distributions are presented in **Table 1**. In summary, NIEND offers the most substantial improvement to automated tracing performance.

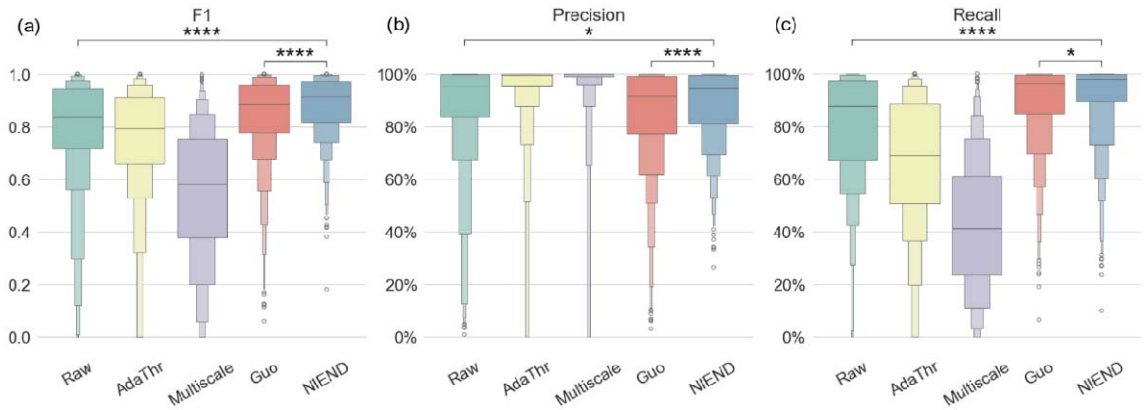

Figure 8. **Quantitative evaluation of automatic tracing performance.** (**a**) F1 score distribution, illustrating the significant enhancement of tracing quality achieved by NIEND, surpassing all others. (**b**) precision score distribution, wherein NIEND exhibits moderate precision, yet with a more focused distribution, implies its reliability. (**c**) recall score distributions, where NIEND matches the exceptional performance of Guo's method, indicating that NIEND's overall superiority over Guo's method can be attributed to its increased and focused precision. Each statistical significance is obtained using the two-sided T-test.

Table 1. Average F1, precision, and recall of benchmarking of different methods

Method	**Average F1↑**	**Average Precision↑**	**Average Recall↑**
Raw	0.7820	86.26%	79.53%
AdaThr	0.7415	93.18%	66.08%
Multiscale	0.5513	95.77%	43.00%
Guo	0.8425	84.67%	89.08%
NIEND	0.8792	88.33%	90.84%

3.4 Ablation study

The ablation study is conducted to assess the contributions from each step in the NIEND process. The results are presented in **Supplementary Table 2**.

First, the images are substituted with 8-bit images. The result shows a considerable drop in recall (22%), which is not surprising because high-pass filtering, as NIEND's first step, can reveal more information from images of greater depth that usually have more high-frequency details.

The ablation of the diffusion filter displays minor variation in F1. It can be explained by the overlap of denoised targets between them. As illustrated in **Supplementary Figure 1b**, the diffusion filter mitigates some of the orthogonal artifacts to a certain degree. This overlap is further confirmed by the 4% decrease in recall when both steps are ablated. On the other hand, without the orthogonal filer, F1 even increases a bit (<0.001), indicating that its improvement and degradation are equally matched in our test samples and it yields little benefits in the presence of the diffusion filter. However, it is still adopted by NIEND for extra robustness against the relatively rare but critical artifacts (**Supplementary Figure 4**).

The instance-aware intensity shifting displays the most significant impact on the performance, with its ablation incurring a substantial 30% decrease in recall. As APP2 is preceded by a linear 8-bit conversion, the image with the original wide intensity range will suffer a huge loss of the

clear but weak foreground left by high-pass filtering. Adaptive thresholding suffers from a considerable decrease in recall (**Figure 8c**) for the same reason.

The ablation of wavelet denoising shows only an insignificant drop. Similar to the orthogonal filter, wavelet denoising uniquely targets rarer but more intractable issues for other techniques. Another unintended consequence of wavelet denoising is the block effect (distorting the surfaces of neurites), an artifact to which some tracing algorithms are sensitive.

3.5 Performance advantage and high compression rate

Apart from the vast improvement in image quality, NIEND also facilitates a considerably low time and memory usage, which is, on average, 29.1s and 1GB per image for our tested cases. For images of a smaller size (256×256×256), they can be reduced to 1.6s and 64MB per image.

The superior SBC and WIV offered by NIEND (**Figure 6a,c**) are also indicative of a high compression rate of the processed neuronal images. To compare the compression rate between different image processing methods, the images are compressed using the LZMA (Lempel–Ziv–Markov chain) algorithm in TIFF format, with compression data presented in **Table 2**. The initial size of each image (16-bit) used in this study is 512MB. Following each processing method, images are all standardized to 8-bit (256MB) and subsequently.

Compression rates are computed as the compressed file size divided by the full file size. Of all the methods, multiscale enhancement achieves the smallest compression size (2.48MB), closely trailed by NIEND (2.49MB). Both methods achieve impressively low compression rates of 1.0%, surpassing all other methods. Considering the abnormally high signal loss of multiscale enhancement, NIEND indisputably emerges as the optimal choice for the efficient storage of petascale image data.

Table 2. Average compression rate for 1891 256MB images using LZMA and V3DPBD compression of different methods

Method	**LZMA Size (MB)↓**	**LZMA Compression Rate↓**	**V3DPBD Size (MB)↓**
Raw	45.3	17.7%	87.2
AdaThr	16.2	6.3%	52.1
Multiscale	2.48	1.0%	8.6
Guo	13.5	5.3%	31.9
NIEND	2.49	1.0%	10.6

In addition, using V3DPBD, a PackBits compression format for multi-dimensional images implemented by Vaa3D (Peng *et al.* 2014) and also incorporated in other software such as ImageJ (Schindelin *et al.* 2012), the images can achieve a less competent compression rate but with a remarkably lower compression/decompression time. For NIEND-processed images, the file size can be reduced to around 4% of the original sizes within seconds.

4 Conclusion and Discussion

In this research, we have proposed a novel pipeline, NIEND, for the enhancement of neuron optical images. It effectively improved the image quality at a low time and memory cost, using a combination of distinct, prior-knowledge-based denoising algorithms to address various types of noise and artifacts resulting from technical flaws in the current sample preparation and imaging system. As a result, it succeeds in facilitating automatic tracing of higher performance and boosting large-scale data storage and share efficiency.

Given the vast amount of imaging data of the mammalian nervous system, there is a significant need for either semi- or fully-automated pipelines for neuron morphology analysis. Numerous attempts have been made to construct such pipelines utilizing cutting-edge computational methods (Gao *et al.* 2022; Li *et al.* 2023). Still, the outcomes of these automated methods often fall short of the manual tracing level in accuracy, owing in part to the image quality issues. Our method emerges as a competent solution for its efficacy and cost-efficiency. Advanced segmentation methods driven by sophisticated models, particularly deep learning models, are also gaining attention and demonstrating substantial potential in the realm of biomedical image processing. Yet their cost is also undeniably high for large-scale 3D biological images.

NIEND benefits the high-speed tracing algorithms the most, the use of which is often limited to high-quality images owing to their simplicity in image analysis (e.g. the thresholding technique of APP2). In low-quality images, noise and artifacts undermine their performance by confusing

their image analysis (**Supplementary Figure 5**), which can be ameliorated with proper measures, e.g. the high-pass filtering of NIEND. Therefore, the combination of NIEND with high-speed tracing algorithms will display a considerably high competence over other sophisticated neuron optical image analysis pipelines.

Despite its simplicity as a band-pass filter, NIEND differentiates itself from other frequency-based methods by not decomposing the signal into a regular frequency space, e.g. Fourier space. Instead, it quantifies patterns of dynamic frequency ranges, drawing inspiration from Empirical Mode Decomposition (Huang *et al.* 1998), a common technique for non-stationary time series signal processing. For neuron optical images, the non-stationary signal can be interpreted as the variable noise and artifacts that alter the local statistical properties, e.g. the APP2 thresholding. This theory coincides with the amelioration depicted in **Supplementary Figure 5**.

The limitations of NIEND also deserve attention. As it is highly specialized for fMOST images, it is not likely to work for other neuron optical images, especially those with different kinds of artifacts, e.g. light-sheet tomography that displays double-sided attenuation noise (Narasimhan *et al.* 2017). Furthermore, some of the steps in NIEND may introduce extra distortions or fail to eliminate all of the artifacts. Therefore, we also hope NIEND can be an inspiration for more powerful image processing approaches in the future.

Funding

This work was supported by the Southeast University initiative of neuroscience; Fundamental Research Funds for the Central Universities [2242023K5005]; Natural Science Foundation of China Guangdong Joint Fund [U20A6005]; and Science and Technology Innovation 2030 Major Projects [2022ZD0205200,2022ZD0205204].

Conflict of Interest: none declared.

Reference

Bernsen J. Dynamic Thresholding of Grey-Level Images. *Proceedings of the Eighth International Conference on Pattern Recognition*. Paris: Computer Society Press, 1986, 1251–5.

Chang SG, Bin Yu, Vetterli M. Adaptive wavelet thresholding for image denoising and compression. *IEEE Trans on Image Process* 2000;**9**:1532–46.

Chernavskaia O, Guo S, Meyer T *et al*. Correction of mosaicking artifacts in multimodal images caused by uneven illumination: Correction of uneven illumination artefacts. *Journal of Chemometrics* 2017;**31**:e2901.

Gao L, Liu S, Gou L *et al.* Single-neuron projectome of mouse prefrontal cortex. *Nat Neurosci* 2022;**25**:515–29.

Gong H, Xu D, Yuan J *et al.* High-throughput dual-colour precision imaging for brain-wide connectome with cytoarchitectonic landmarks at the cellular level. *Nat Commun* 2016;**7**:12142.

Gong H, Zeng S, Yan C *et al.* Continuously tracing brain-wide long-distance axonal projections in mice at a one-micron voxel resolution. *NeuroImage* 2013;**74**:87–98.

Guo S, Zhao X, Jiang S *et al.* Image enhancement to leverage the 3D morphological reconstruction of single-cell neurons. Vitek O (ed.). *Bioinformatics* 2022;**38**:503–12.

Halidou A, Mohamadou Y, Ari AAA *et al.* Review of wavelet denoising algorithms. *Multimed Tools Appl* 2023, DOI: 10.1007/s11042-023-15127-0.

Hayman MW, Smith KH, Cameron NR *et al*. Enhanced neurite outgrowth by human neurons grown on solid three-dimensional scaffolds. *Biochemical and Biophysical Research Communications* 2004;**314**:483–8.

Huang NE, Shen Z, Long SR *et al*. The empirical mode decomposition and the Hilbert spectrum for nonlinear and non-stationary time series analysis. *Proc R Soc Lond A* 1998;**454**:903–95.

Jiang T, Gong H, Yuan J. Whole-brain Optical Imaging: A Powerful Tool for Precise Brain Mapping at the Mesoscopic Level. *Neurosci Bull* 2023, DOI: 10.1007/s12264-023-01112-y.

Li A, Gong H, Zhang B *et al*. Micro-optical sectioning tomography to obtain a high-resolution atlas of the mouse brain. *Science* 2010;**330**:1404–8.

Li Z, Shang Z, Liu J *et al*. D-LMBmap: a fully automated deep-learning pipeline for whole-brain profiling of neural circuitry. *Nat Methods* 2023, DOI: 10.1038/s41592-023-01998-6.

Liu Y, Wang G, Ascoli GA *et al*. Neuron tracing from light microscopy images: automation, deep learning and bench testing. Peng H (ed.). *Bioinformatics* 2022:btac712.

Meijering E. Neuron tracing in perspective. *Cytometry Pt A* 2010;**77A**:693–704.

Mukherjee S, Acton ST. Oriented filters for vessel contrast enhancement with local directional evidence. *2015 IEEE 12th International Symposium on Biomedical Imaging (ISBI)*. Brooklyn, NY, USA: IEEE, 2015, 503–6.

Narasimhan A, Venkataraju KU, Mizrachi J *et al*. *Oblique Light-Sheet Tomography: Fast and High Resolution Volumetric Imaging of Mouse Brains*. Neuroscience, 2017.

Peng H, Bria A, Zhou Z *et al*. Extensible visualization and analysis for multidimensional images using Vaa3D. *Nat Protoc* 2014;**9**:193–208.

Peng H, Hawrylycz M, Roskams J *et al*. BigNeuron: Large-Scale 3D Neuron Reconstruction from Optical Microscopy Images. *Neuron* 2015;**87**:252–6.

Peng H, Long F, Myers G. Automatic 3D neuron tracing using all-path pruning. *Bioinformatics* 2011;**27**:i239–47.

Peng H, Xie P, Liu L *et al*. Morphological diversity of single neurons in molecularly defined cell types. *Nature* 2021;**598**:174–81.

Peng T, Thorn K, Schroeder T *et al*. A BaSiC tool for background and shading correction of optical microscopy images. *Nat Commun* 2017;**8**:14836.

Qi Y, Yang Z, Sun W *et al*. A Comprehensive Overview of Image Enhancement Techniques. *Arch Computat Methods Eng* 2022;**29**:583–607.

Schindelin J, Arganda-Carreras I, Frise E *et al*. Fiji: an open-source platform for biological-image analysis. *Nat Methods* 2012;**9**:676–82.

Smith K, Li Y, Piccinini F *et al*. CIDRE: an illumination-correction method for optical microscopy. *Nat Methods* 2015;**12**:404–6.

Wang X, Xiong H, Liu Y *et al.* Chemical sectioning fluorescence tomography: high-throughput, high-contrast, multicolor, whole-brain imaging at subcellular resolution. *Cell Reports* 2021;**34**:108709.

Xiao H, Peng H. APP2: automatic tracing of 3D neuron morphology based on hierarchical pruning of a gray-weighted image distance-tree. *Bioinformatics* 2013;**29**:1448–54.

Zhong Q, Li A, Jin R *et al*. High-definition imaging using line-illumination modulation microscopy. *Nat Methods* 2021;**18**:309–15.

Zhou Z, Sorensen S, Zeng H *et al.* Adaptive Image Enhancement for Tracing 3D Morphologies of Neurons and Brain Vasculatures. *Neuroinform* 2015;**13**:153–66.

Zhu X, Xia Y, Wang X *et al.* Optical Brain Imaging: A Powerful Tool for Neuroscience. *Neurosci Bull* 2017;**33**:95–102.